Bi-phase metallic cobalt with efficient broadband absorption in X and Ku bands

Jing Zhang[1] · Yuchang Su[1] · Hongzhi Zhang[1] · Libo Wang[1] · Qiushan Yu[1]

Abstract

Broadband and lightweight microwave absorbers have gained considerable research interest in overcoming electromagnetic interference pollution. Here, mixture of two phase (fcc and hcp) metallic cobalt powders with broadband absorption was synthesized through solvothermal method using ethylene glycol as the reducing agent. The effect of NaOH content on the structure and morphology of the prepared Co powders is investigated by X-ray diffraction and field-emission scanning electron microscopy. Ring samples of 7.00/3.04 mm of out/inner diameter were prepared with paraffin for microwave absorption testing by vector network analyzer. It was observed that the increase of NaOH content caused a relative higher generation of hcp-Co phase and formation of irregular microspheres. The reflection loss (RL) peak and effective absorbing bandwidth (EABW, $RL \leq -10$ dB) shifted towards lower frequency when the sample thickness increased from 1.00 to 3.00 mm with EABW covering almost all the C, X and Ku bands (4–18 GHz). The bi-phase Co prepared in a low base solution exhibited enhanced microwave absorption properties. The width of largest EABW has reached 6.33 GHz covering partial Ku band and almost all the X band with optimal RL of −56.95 dB at a sample thickness of only 1.85 mm, which is superior to EABW of Co crystals reported earlier. We proposed that such a wide EABW is due to the fact of Z values closed to 1.0 ($0.8 \leq |Z| \leq 1.2$) at almost the whole frequency range. This indicates that the prepared bi-phase Co powders are excellent microwave absorbers with large bandwidth, have good prospects.

1 Introduction

Owing to its efficiency and convenience, radio wave technology has garnered considerable attention in various fields such as national defense, communication, transportation, medicine and so on. However, electromagnetic (EM) irradiation is not only harmful to human health but also poses a security risk in military applications [1–3]. Therefore, it is of great significance to explore electromagnetic wave absorbing materials (EMWAMs) in GHz range for restricting EM pollution, avoiding shielding interference in electronic devices, and enhancing stealth technology in military field to avoid radar detection. Consequently, enormous efforts have been devoted to different kinds of high-performance EMWAMs, which could effectively absorb unwanted EM waves or/and dissipate them by interference, such as dielectric/magnetic materials, carbon base materials, organic polymers and their composites [4–9]. Ideally EMWAMs should be light weight, ultra-thin, strong absorbers with broad absorption bandwidth [10, 11].

Cobalt is a representative ferromagnetic material, which has potential applications in magnetic fluids, high-density information storage, magnetic sensors, catalysis, and microwave absorption [12–14]. Due to their high saturation magnetization, relatively high temperature resistance and corrosion resistance [15], Co powders have been good candidates for EMWAMs. Although many kinds of Co morphologies have been prepared via reduction methods, including dendritic shape, rings, flower-like spheres, etc. [16–20], the efficient broadband absorption of Co has been rarely reported. Co possesses three types of structures, namely, hcp phase (hcp-Co), fcc phase (fcc-Co), and pseudo-cubic phase (pseudo-cubic-Co), and the first two are more stable than the latter [21]. The eddy current induced in metallic Co is not conducive to impedance matching, causes stronger reflection

✉ Yuchang Su
ychsu@csu.edu.cn

[1] School of Materials Science and Engineering, Central South University, Changsha 410083, People's Republic of China

of EM wave. It has been reported that Co with modified morphology can reduce the conductivity [22]. However, it is a major challenge to balance impedance matching and attenuation. In particular, the realization of better impedance matching with efficient broadband absorption is highly desired.

Typically, ethylene glycol (EG, boiling point 197 °C) is simultaneously used as a solvent and reducing agent to prepare metallic powders [23–25]. The reducibility of EG is strongly associated with NaOH concentration. In particular, a high NaOH concentration facilitates the reduction reaction [26, 27]. However, most of the earlier studies on the synthesis of Co with various morphologies used reducing agents, such as hydrazine hydrate ($N_2H_4 \cdot H_2O$), sodium borohydride ($NaBH_4$), and sodium hypophosphite (NaH_2PO_2), and very few used EG. The utilization of EG as the reducing agent is simple and convenient; however, the relationship between morphologies, structures, and EM parameters of metallic Co reduced by EG has been rarely investigated.

In this study, we synthesize metallic Co powders with efficient broadband absorption through solvothermal method, with EG as both solvent and reducing agent. We have investigated the effects of NaOH content on the structure and morphology of the synthesized Co powders and their microwave absorption performance. We have confirmed that these powders exhibit strong absorption and large absorption bandwidth at small thickness. Their phases, morphologies, static magnetic properties, and electromagnetic parameters are also characterized.

2 Experimental

2.1 Raw materials

The Co metals were prepared using the following raw materials: cobalt chloride hexahydrate ($CoCl_2 \cdot 6H_2O$, purity 99%), trisodium citrate dihydrate ($Na_3C_6H_5O_7 \cdot 2H_2O$, purity 99%) as the complexing agent, sodium hydroxide (NaOH, purity 96%) as the alkali source to adjust the pH of the environment, and EG ($C_6H_6O_2$, purity 99%) as both solvent and reducing agent, which are all analytical grade chemical reagents.

2.2 Synthesis of Co samples

Firstly, 4 mmol $CoCl_2 \cdot 6H_2O$ and 6 mmol $Na_3C_6H_5O_7 \cdot 2H_2O$ were dissolved in 45 mL EG in sequence, and 100 mmol NaOH was dissolved in 50 mL EG. These solutions were stirred until they became homogeneous. Subsequently, NaOH solution was poured into the salt solution with vigorously magnetic stirring for 2 h at 50 °C. Then, 85 mL mixed solution was taken out and transferred into Teflon-lined

autoclave. This solution was kept at 200 °C for 24 h, and naturally cooled down to room temperature. Finally, the obtained dark grey precipitates were washed four times with distilled water and alcohol, and dried in an oven at 80 °C for 12 h. The final samples were labeled as S1. Follow the same steps, replacing NaOH content 100 mmol with 60, 32, and 8 mmol, respectively, and resultant samples were named as S2, S3 and S4.

2.3 Characterization

The crystal structure of the samples was analyzed by X-ray diffraction (XRD, D/max 2550 VB, 40 kV/450 mA). The morphology was characterized by field-emission scanning electron microscopy (FSEM, SIRION200, at 200 kV) equipped with energy dispersive X-ray spectrometer (EDS). The magnetic parameters such as saturation magnetization (M_s), coercivity (H_c) and remanent magnetization (M_r) were detected by vibrating sample magnetometer (VSM, Lake Shore 7307) at room temperature in a maximum applied field of 10,000 Oe. Ring samples of 7.00/3.04 mm of out/inner diameter were prepared with paraffin. The microwave absorption testing in the 2–18 GHz frequency range was accomplished by a vector network analyzer (VNA, AV3672B-S).

3 Results and discussion

Figure 1a presents XRD patterns of the as-prepared samples S1–S4. The five obvious diffraction peaks at $2\theta = 41.6$, 44.4, 47.4, 51.5 and 75.9° indicate the coexistence of two phases i.e., hcp-Co and fcc-Co. The peaks located at $2\theta = 41.6$, 44.2, 47.4 and 75.9° primarily correspond to (101), (002), (100) and (110) crystal planes of hcp-Co (JCPDS card no. 89-7373). The peaks located at $2\theta = 44.5$, 51.5 and 75.9° mainly correspond to (111), (200) and (220) crystal planes of fcc-Co (JCPDS card no. 89-4307). The spectra of these samples obtained from EDS in Fig. 1b and Fig. S1 (Supporting information) indicate that the prepared samples are essentially pure Co, which is consistent with the XRD results. A small amount of oxygen element may be attributed to the adsorption of oxygen or partial oxidation on the surface of Co. Compared with XRD pattern of S1, the peaks corresponding to (100), (101), and (200) crystalline planes in S2–S4 are relatively broader, especially the peak for (101) crystalline plane. That may be attributed to the smaller grain size or the relatively large number of stacking faults in (101) plane. As both the hcp and fcc phases are closely packed, the order of atom stacking is only different in the [111] direction [16]. Variations in the parameters of the reaction environment can cause the phase transition between hcp-Co and fcc-Co, and therefore the stacking faults are formed [14], which is one of the reasons for the broadening of the diffraction peak.
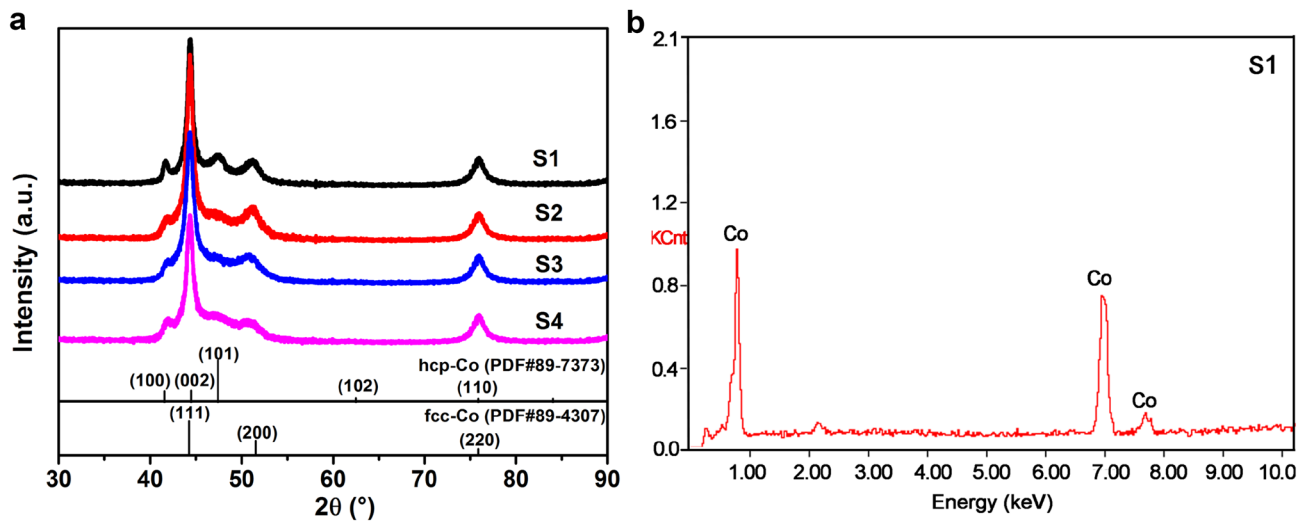
Fig. 1 **a** XRD patterns of samples prepared at different NaOH content: S1 (100 mmol), S2 (60 mmol), S3 (32 mmol), S4 (8 mmol); **b** EDS spectrum of sample S1

Table 1 The weight ratio of hcp-Co and fcc-Co for samples S1–S4

Samples	S1	S2	S3	S4
hcp-Co content/%	50.1	48.9	37.4	34.2
fcc-Co content/%	49.9	51.1	62.6	65.8

The calculated weight ratio of hcp-Co and fcc-Co are shown in Fig. S2 and summarized in Table 1. The content of hcp-Co increases at higher NaOH concentrations, which is consistent with the larger H_c values in Table 2 (the magnetocrystalline anisotropy of hcp-Co is larger than that of fcc-Co [28]). The crystallinity of S1 is better than that of S4, which may be associated with the fewer stacking faults in S1. The existence of stacking faults is propitious for improving interfacial polarization, which enhances the dielectric losses.

Figure 2 shows the FSEM images of Co powders at different magnifications. It is evident that the prepared Co samples mainly consist of microspheres and ball-chains. The ball-chains are assembled by microspheres via the magnetic interaction. The morphologies become more irregular as the NaOH concentration increases. Figure 2a and b exhibit the morphology of S1, whose surface is rough and composed of a huge number of nanoparticles. The morphology of S2 is similar to that of S3. Nanoparticles randomly diffuse and grow into nanosheets, and assembled into flower-like microspheres

by interfacial tension and hydrophilic surfaces [18]. S4 is comprised of microspheres with smooth surface, as shown in in Fig. 2g and h. This different morphology can be attributed to the NaOH concentration and the viscosity of solvent. The strong concentration of base solution promotes reducing reaction [27], and relatively large amounts of Co^{2+} are reduced. At the onset of reaction, the viscosity of solvent was high, which limited the diffusion of Co nuclei, consequently microspheres consisting of nanoparticles were formed. The viscosity of solvent decreased rapidly as the reaction proceeded, and the diffusion of Co nuclei became easier, leading to fractal growth and irregular morphology. On the contrary, the reducing ability of EG was weakened at lower concentrations of base solution [26], the amount of reduced Co^{2+} was less, and the viscosity of solvent was relatively high. The high viscosity in solvent inhibited the diffusion of Co nuclei [28], and nanoparticles assembled and grew together, hence spherical particles with smooth surface were formed.

Figure 3 presents the *M*–*H* hysteresis loops of S1–S4. The slender 'S' shape implies that as-prepared metallic cobalt powders exhibit ferromagnetism. As shown in magnified magnetization curves in the magnetic field range of 8–9 kOe, the magnetization value is not fully saturated. M_s can be calculated using the following equation [29]:

$$M = M_s(1 - k/H) \qquad (1)$$

Table 2 The magnetic parameters of S1, S2, S3, S4 and representative Co samples

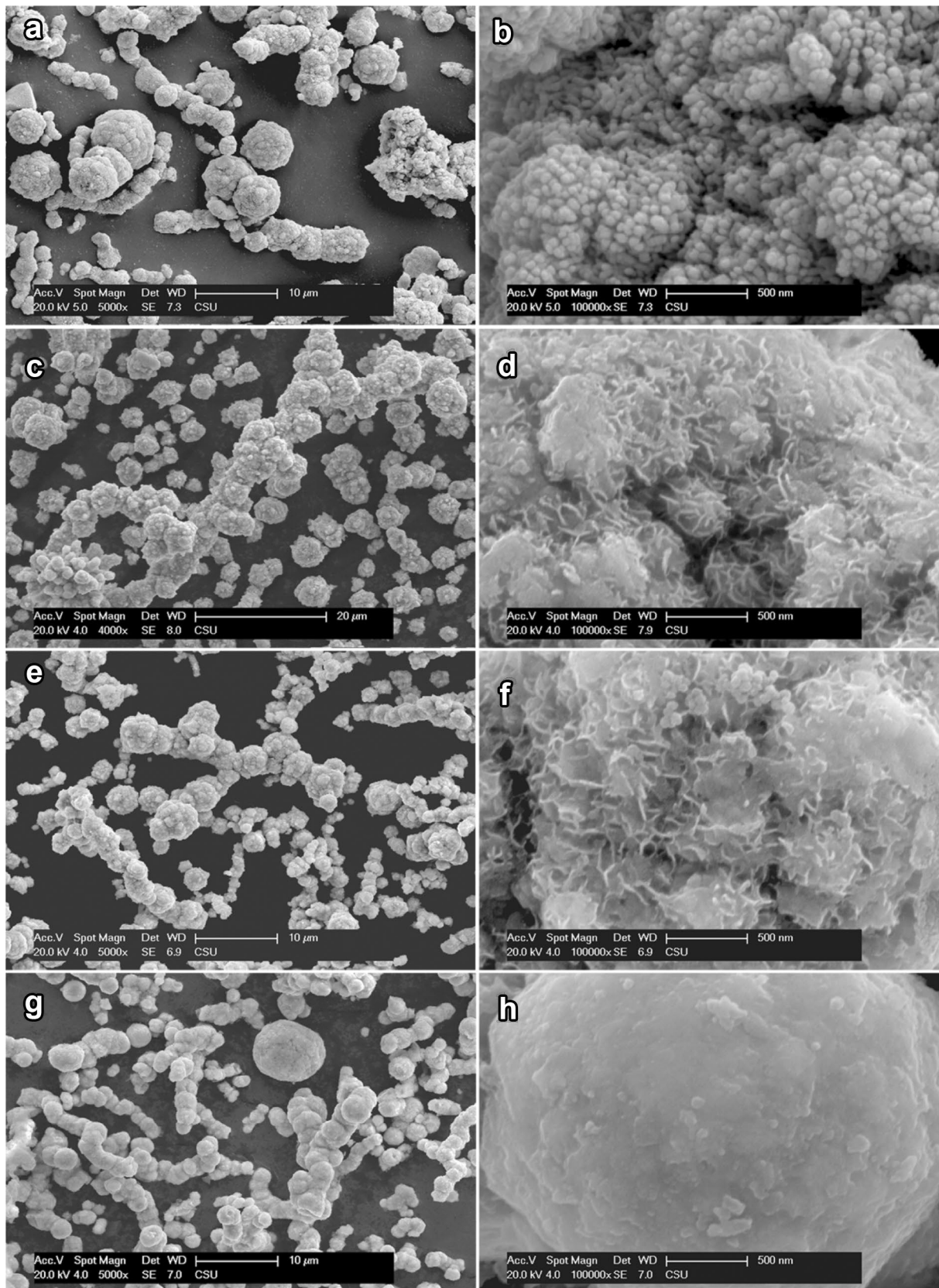| Sample	S1	S2	S3	S4	Ref. [33]	Ref. [34]	Ref. [35]	Ref. [36]
M_s (emu/g)	159.87	152.50	151.10	151.20	137	142	155.39	123
H_c (Oe)	79.23	66.57	65.63	60.04	168	343.2	174.13	176
M_r (emu/g)	6.08	4.41	5.52	5.45	–	–	–	–

Fig. 2 FSEM images of sample **a**, **b**: S1, **c**, **d**: S2, **e**, **f**: S3, and **g**, **h**: S4. The images on the right correspond to higher magnification
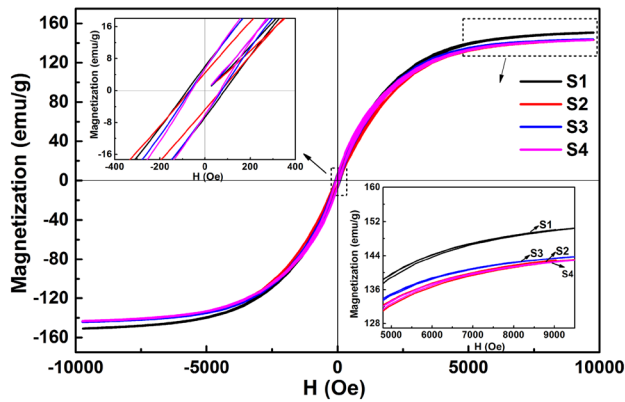
Fig. 3 M–H hysteresis loops of the four samples. The insets show the magnified response in the regions enclosed by dotted rectangles

where k is the fitting parameter. The calculated M_s values of S1, S2, S3, and S4 samples are 159.87, 152.50, 151.10 and 151.20 emu/g, respectively. The H_c values read from the magnified plots in the $-400-400$ Oe magnetic field range are 79.23, 66.57, 65.63 and 60.04 Oe, respectively. The lowest value of M_s and H_c for the sample S4 can be ascribed to the larger number of stacking faults and less shape anisotropy, respectively. The samples S1–S4 exhibit larger M_s and smaller H_c values than that reported for Co in the existing literature (Table 2). The high M_s values contribute to increasing permeability in GHz frequency range, which could effectively improve impedance matching, according to the Snoek's limit expressed as follows [30]:

$$(\mu_i - 1)f_r = \gamma M_s/3\pi \qquad (2)$$

where μ_i represents the real part of permeability, f_r is the resonant frequency and γ is the gyromagnetic ratio. The values of M_s for the samples S1–S4 are smaller than that for bulk Co (168 emu/g [31]). This may be ascribed to the pinning effect of citrate ions or oxygen atoms attached on the surface of cobalt microspheres, resulting in the reduced number of effective Bohr magnetons [32]. H_c values for S1–S4 are larger than that for bulk Co (10 Oe [31]), which can be attributed to shape anisotropy, stacking faults and interfaces between hcp-Co and fcc-Co. This inhibits magnetic domain from moving and magnetic moment rotating, and thus more magnetic energy are required [20].

The EM wave absorbability of materials can be characterized by the reflection loss (RL), which is determined by the relative complex permittivity (ε_r) and permeability (μ_r), frequency (f) and thickness (d) of absorbers. Both ε_r ($\varepsilon_r = \varepsilon' - i\varepsilon''$) and μ_r ($\mu_r = \mu' - i\mu''$) comprises real and imaginary parts, where ε' (ε'') and μ' (μ'') represent the storage (loss) of electric and magnetic energies, respectively. The dielectric loss tangent ($tan\delta_e = \varepsilon''/\varepsilon'$) and magnetic loss

tangent ($tan\delta_m = \mu''/\mu'$) can be used to evaluate the microwave attenuation capacity of the materials [37].

Figure 4a–d shows the frequency dependence of ε_r, μ_r, $tan\delta_e$, and $tan\delta_m$ for S1–S4 samples mixed with paraffin (containing 80 wt% Co + 20 wt% paraffin), respectively. The ε' and ε'' values vary accompanying with some downward concave peaks and upward convexity peaks, as depicted in Fig. 4a. ε' of S1–S3 is higher than that of S4 in the 2–8.5 and 13–18 GHz range. ε'' values of S1–S3 is larger than that of S4 in most frequency range. The phenomenon may be attributed to structural heterogeneity and uneven space charges distribution [38]. S1–S3 contain more interfaces than S4 in samples mixed with paraffin. The interfaces between cobalt and wax as well as that between hcp-Co and fcc-Co hinder charges' motion to varying degrees, giving rise to more interfacial polarization. ε'' is approximately proportional to conductivity σ ($\varepsilon'' \approx \sigma/\omega\varepsilon_0$) [39], and the high σ value is detrimental to impedance matching. S1–S3 exhibits larger ε'' values than S4, implying poor impedance matching in the latter. It may be noted that the variation trend of $tan\delta_e$ is concordant with that of ε'', and the resonant peaks corresponding to ε'' are mainly located at 2.8, 5.2, 7.0, 9.5, 13.0, and 17.2 GHz, which can be attributed to the dielectric loss. The dielectric polarization mainly stems from ionic and electronic polarization, intrinsic dipole orientation polarization, and interfacial polarization [40], causing the dielectric loss in the alternating EM field. As the resonant peaks corresponding to the ionic and electronic polarization are usually in the THz and PHz range [41], the resonant peaks of the prepared Co can be attributed to dipole orientation polarization and interfacial polarization. The variation of interfaces and stacking faults would alter the extent of space charges accumulation, causing the dipole orientation polarization and interfacial polarization.

Figure 4b shows the variation of μ_r as a function of f. μ' decreases with the increase in frequency and approaches 1.0 at high frequency, presenting good frequency dispersion behavior. μ'' exhibits a decreasing trend with six obvious resonant peaks at 4.5, 6.5, 8.0, 10.5, 12.3 and 14.7 GHz, which are associated with strong magnetic losses. Figure 4d displays the frequency dependency of $tan\delta_m$, and the resonant peaks in $tan\delta_m$ are consistent with that of μ''. The magnetic losses are mainly from hysteresis loss, domain wall resonant loss, eddy current loss, natural and exchange resonant loss [42]. The hysteresis loss can be ignored in a weak applied field, and domain wall resonant loss usually appears at 1–100 MHz [43]. If the eddy-current loss is dominant, C_0 ($C_0 = \mu''(\mu')^{-2}f^{-1}$) becomes a constant and therefore is not affected by frequency [44]. Figure 5 plots the relationship between C_0 and f. C_0 exhibits a decreasing tendency with six fluctuation peaks. The peak position of C_0 is consistent with that of $tan\delta_m$. This indicates that it is natural resonant and exchange resonant losses rather than eddy-current loss that play a leading role in magnetic
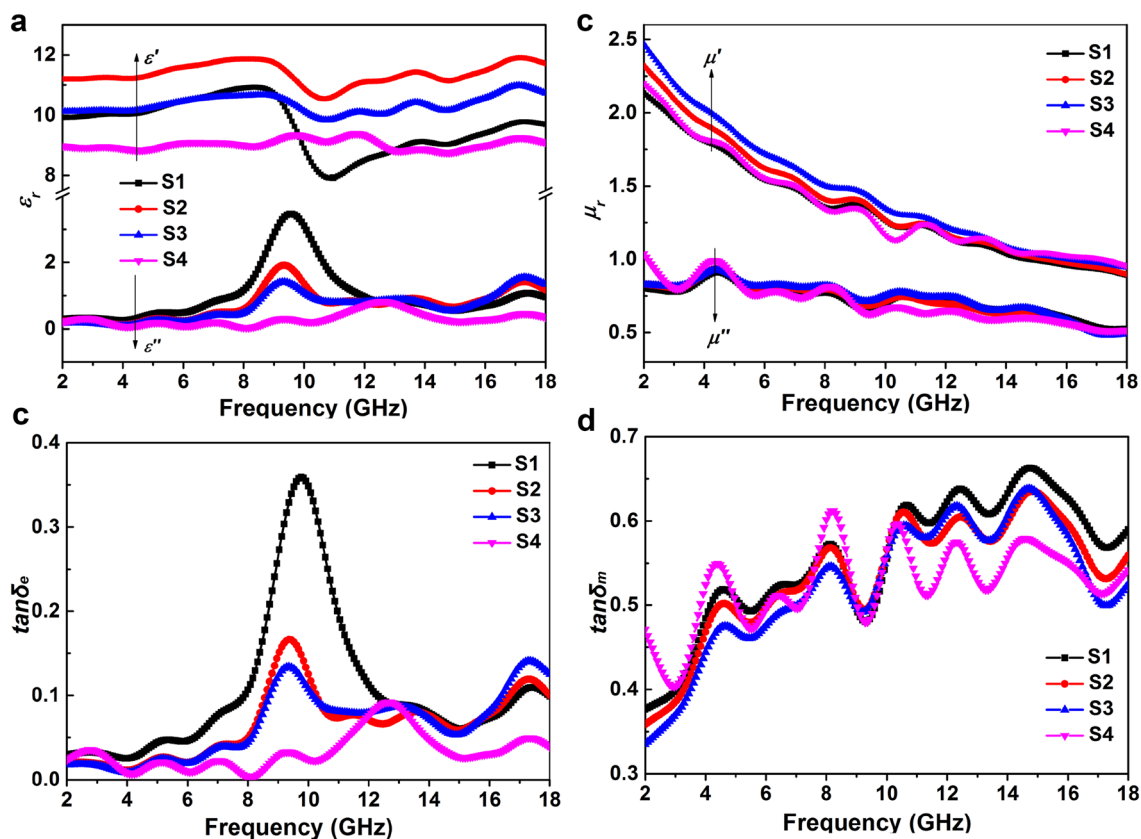
Fig. 4 Frequency dependence of ε_r (**a**), μ_r (**b**), $tan\delta_e$ (**c**) and $tan\delta_m$ (**d**) for S1, S2, S3 and S4 samples mixed with paraffin in the range of 2–18 GHz
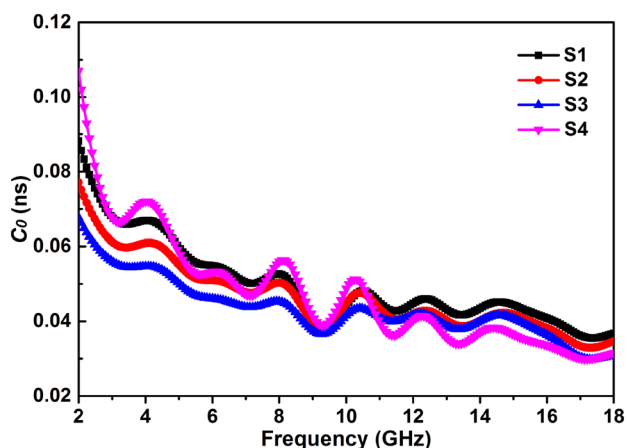

Fig. 5 Frequency dependence of C_0 (μ'' $(\mu')^{-2} f^{-1}$) for S1, S2, S3 and S4 samples mixed with paraffin

loss of hcp-Co/fcc-Co. As reported in an earlier study [45], the natural resonant frequency (f_{nat}) of hcp-Co is 6.5 GHz. f_{nat} of fcc-Co is less than 6.5 GHz as a result of the lower magnetocrystalline anisotropy field. Therefore, the resonant peaks at 4.5 and 6.5 GHz in Fig. 4d correspond to natural resonant peak

of fcc-Co and hcp-Co, respectively. The exchange resonant frequency (f_{exch}) is closely related to the morphology of Co [40]. As earlier reported, f_{exch} of Co nanoplatelets [46], nanochains [47], nanoflakes [48] and superstructural particles [35] appear in 11.6 GHz, 14.5 GHz, 7.79 and 12.00 GHz, 10.98 and 15.32 GHz, respectively. Hence, the peaks at 8.0, 10.5, 12.3 and 14.7 GHz could be attributed to exchange resonant peaks. The μ'' values of S1–S3 are higher than that of S4 at high frequencies, which might be due to the larger amounts of magnetic nanoparticles/nanosheets. The coexistence of natural and exchange resonance is of benefit in increasing the microwave absorption bandwidth [35]. It is evident that $tan\delta_m$ is distinctly larger than $tan\delta_e$, which demonstrates that the magnetic loss plays a more crucial role in microwave absorption than dielectric loss. The synergistic action of dielectric and magnetic losses could promote strong microwave attenuation.

According to transmission line theory, the theoretical *RL* values could be calculated using the following equations [6]:

$$RL(dB) = 20 \log \left| (Z_{in} - Z_o)/(Z_{in} + Z_o) \right| \tag{3}$$

$$Z = Z_{in}/Z_0 = \sqrt{\mu_r/\varepsilon_r} \tanh[j(2\pi f d/c)\sqrt{\mu_r \varepsilon_r}] \tag{4}$$

where Z_0 and Z_{in} represent the free space impedance and input impedance of absorbers respectively. $Z (= Z_{in}/Z_0)$ is constant for a given f and d. When Z_0 and Z_{in} satisfy the impedence matching condition, $|Z| = 1.0$, implying that the incident EM wave is completely absorbed. The optimal RL and Z can be acquired by altering f and d.

Figure 6 displays the 3D plots and contour maps of RL for S1–S4. The white short dash lines represents $RL = -10$ dB. In the surrounding region of these curves, $RL < -10$ dB, implying that more than 90% EM wave energy is attenuated. The length of red dashed line represents the effective absorption bandwidth (EABW, corresponding to $RL \leq -10$ dB) at optimum matching thickness (d_m). In addition to the minimum RL (RL_{min}), EABW is another important parameter that determines the performance of microwave absorbers. It is apparent in Fig. 6 (for the same sample) that RL peak and EABW move towards low frequency direction with increasing thickness d. When d varies between 1.00 and 3.00 mm, EABW covers almost all C, X and Ku bands (4–18 GHz), i.e., it covers 87% of the bands in 2–18 GHz range. Figure 7 (2D plots) shows RL vs f for samples S1–S4, where d ranges from 1.00 to 3.00 mm. For sample S1 with layer thickness of 2.58 mm, $RL_{min} = -49.89$ dB at 6.64 GHz and EABW = 3.27 GHz. For S2, $RL_{min} = -50.06$ dB at 7.04 GHz, $d_m = 2.29$ mm, and EABW = 3.56 GHz. It is evident that EM absorption performance is significantly improved for S3 and S4. The RL_{min} and d_m of S3 are -66.59 dB and 2.13 mm, respectively, and its EABW is 4.64 GHz. For S4 with a thickness of just 1.85 mm, we achieved an optimal RL of -56.95 dB with EABW of 6.33 GHz. EABW (at optimal matching thickness d_m) of S1, S2, and S3 merely covers partial C and X bands, while that of S4 covers partial Ku band and nearly all the X band. The microwave absorption properties (particularly EABW) of the prepared Co samples are much superior to that reported for other Co-based samples (Table 3).

The obtained RL_{min} values of -49.89, -50.06, -66.59 and -56.95 dB for S1–S4 can be attributed to satisfying simultaneously 1/4 λ interference cancellation theory and impedance matching ($Z = 1.0$), displayed in Fig. 7. The 1/4 λ theory can be expressed as follows [49]:

$$T_m = nc \left/ \left(4f \sqrt{|\varepsilon_r \mu_r|} \right) \right. (n = 1, 3, 5, 7 \ldots) \quad (5)$$

The thickness d corresponding to RL peak is consistent with the theoretical T_m value in Fig. 7.

The superior microwave absorption properties are governed by impedance matching and attenuation constant α. In particular, Z is a crucial factor for achieving efficient broadband absorption. If the impedance matching is poor, even strong attenuation capacity is not sufficient

for attaining desirable EABW [39]. Figure 8 shows the contour maps of $|Z|$ at different f and d, where the black dashed lines represent $|Z| = 1.0$, which signify no reflection of EM wave. The Z values ($0.8 \leq |Z| \leq 1.2$) of S1–S3 are distributed in a narrow frequency range (S1, S2: 2–9 GHz, S3: 2–13 GHz), while that of S4 is distributed in a wider frequency range of 2–18 GHz. The broad distribution of $|Z| \sim 1.0$ is attained because the complex permittivity of S4 is much closer to the complex permeability in a broad frequency range.

The attenuated EM wave energy can be characterized in terms of attenuation constant α, expressed as follows [15]:

$$\alpha = \frac{\sqrt{2}\pi f}{c} * \sqrt{(\mu''\varepsilon'' - \mu'\varepsilon') + \sqrt{(\mu'\varepsilon'' + \mu''\varepsilon')^2 + (\mu''\varepsilon'' - \mu'\varepsilon')^2}} \quad (6)$$

Figure 9 shows the variation of α as a function of f. It is evident that α increases with f except for few fluctuation peaks. Although the attenuation loss α of S4 is smaller than that of S1–S3 in the frequency range 5–18 GHz, EABW of S4 attains a maximum value of 6.33 GHz. Such a wide EABW is due to the fact of Z values closed to 1.0 ($0.8 \leq |Z| \leq 1.2$) at almost the whole frequency range (2–18 GHz).

4 Conclusions

We synthesized metallic Co powders with flower-like or smooth microspheres and ball-chains morphology through solvothermal method using ethylene glycol as both solvent and reducing agent. These Co samples were composed of hcp and fcc phases. The increase of NaOH content caused a relatively larger generation of hcp-Co phase and formation of irregular microspheres.

The experiments and theoretical calculations confirmed that if d is varied between 1.00 and 3.00 mm, EABW covers almost all C, X, and Ku bands (4–18 GHz), i.e., it covers 87% of the bands in 2–18 GHz range. We obtained RL_{min} of -66.59 dB at 8.0 GHz for Co with flower-like microspheres. The optimal value of RL was -56.95 dB at 11.04 GHz for Co with smooth microspheres. The largest EABW was obtained as 6.33 GHz (from 8.18 to 14.51 GHz) covering partial Ku band and almost all the X band. This efficient broadband absorption is attributed to better impedance matching, i.e., the large EABW is obtained because $Z \sim 1$ ($0.8 \leq |Z| \leq 1.2$) in a wide frequency range. The prepared bi-phase metallic Co powders exhibit broadband microwave absorption compared to previously reported Co-based absorbers, and can be used for wide practical applications.
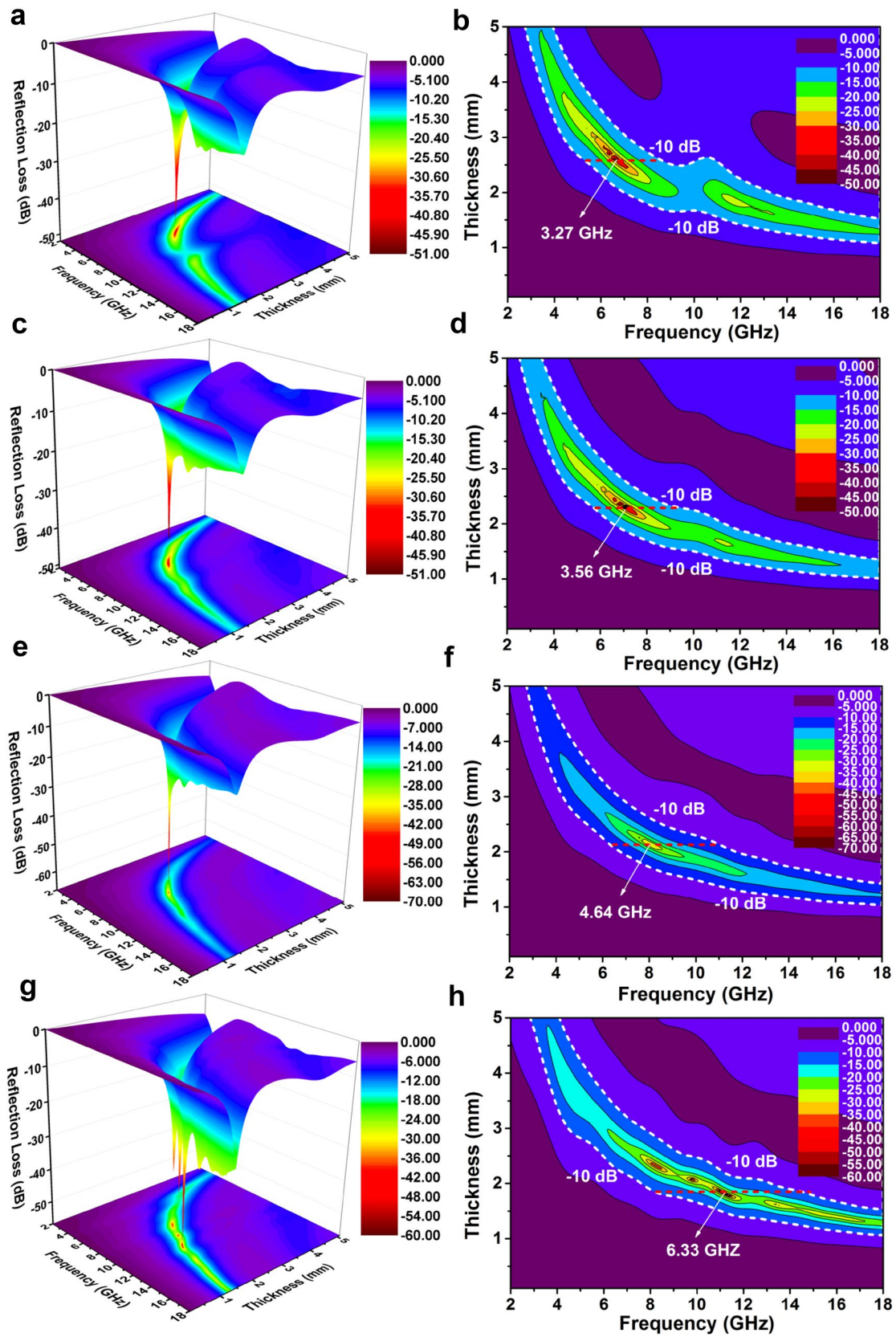
Fig. 6 3D plots (left) and contour maps (right) of reflection loss for sample **a**, **b**: S1, **c**, **d**: S2, **e**, **f**: S3, and **g**, **h**: S4
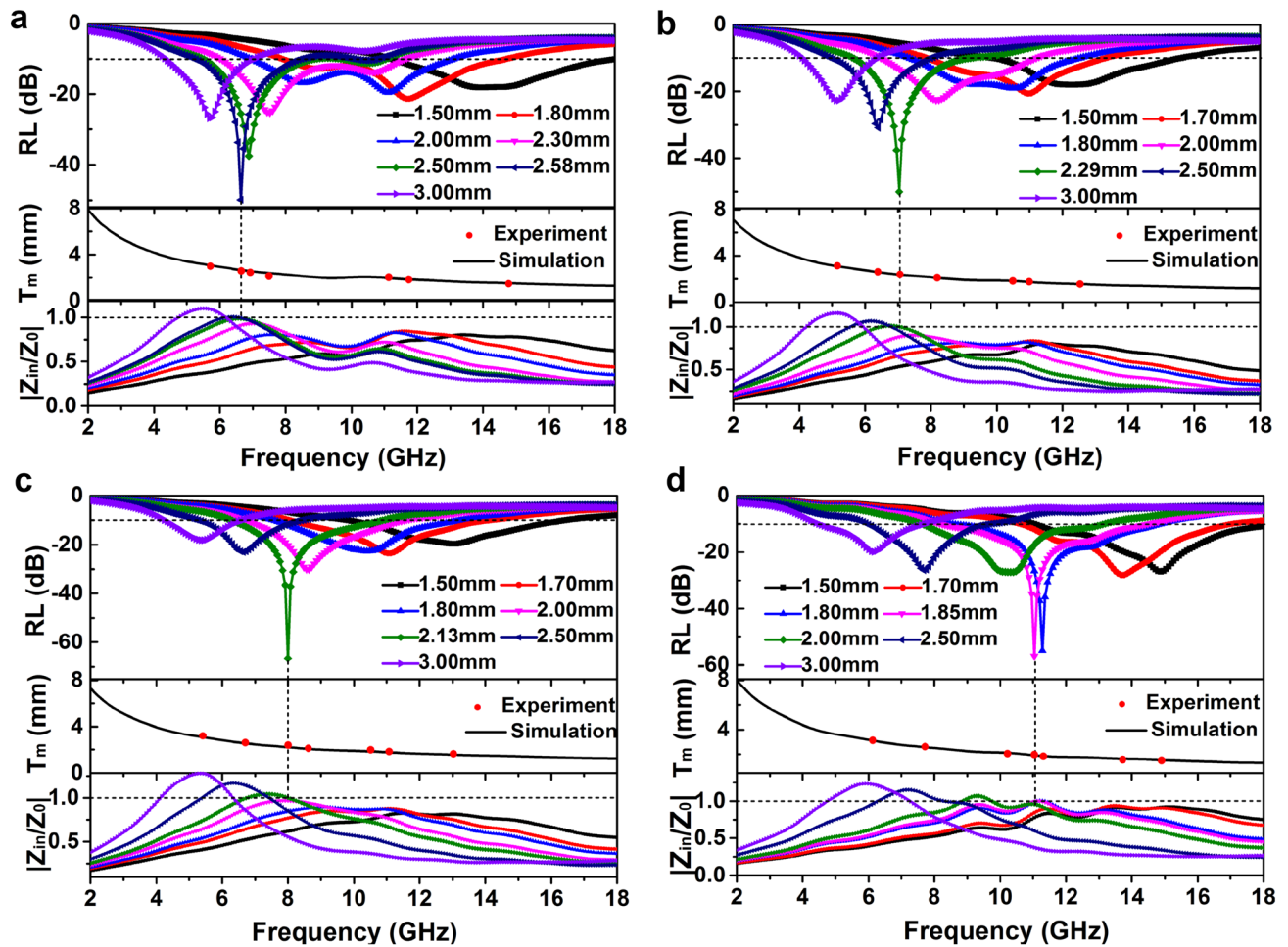
Fig. 7 Frequency dependence of RL, simulation thickness T_m and $|Z_{in}/Z_0|$ for sample **a**: S1, **b**: S2, **c**: S3, and **d**: S4. The numbers in front of the legends indicate sample thickness

Table 3 Microwave absorption parameters for the prepared Co samples S1–S4 and the representative cobalt-based samples

| Sample	Optimal RL (dB)	D_m (mm)	F_m (GHz)	F range RL ≤ − 10 dB (GHz)	EABW in total (GHz)	EABW in C band (GHz)	EABW in X band (GHz)	EABW In Ku band (GHz)	Refs.
Co microspheres	− 19.06	5.0	17.42	16.15–18.00	1.85	–	–	1.85	[32]
Co superstructure	− 77.29	1.5	11.33	9.85–13.45	3.6	–	2.15	1.45	[35]
Co particles	− 13.2	5.5	12.4	~11.7–13.3	1.6	–	~0.3	~1.3	[36]
Co nanochains	− 11.0	3.5	14.5	~14.25–4.75	~0.5	–	–	~0.5	[47]
Sword-like Co	− 60.13	1.4	13.72	~11.0–16.5	5.42	–	~1.0	~4.5	[50]
Flower-like Co@CoO	− 30.4	1.5	16.1	13.4–18.0	4.6	–	–	4.6	[22]
Co@CoO nanocrystals	− 30.5	1.7	14.2	12.6–17.3	4.7	–	–	4.7	[42]
Co/CoO micro-rods	− 48	1.76	8.08	6.8–9.7	2.9	1.2	1.7	–	[49]
S1	− 49.89	2.58	6.64	5.23–8.50	3.27	2.77	0.50	–	This work
S2	− 50.06	2.29	7.04	5.63–9.19	3.56	2.37	1.19	–	This work
S3	− 66.59	2.13	8.00	6.27–10.91	4.64	1.73	2.91	–	This work
S4	− 56.95	1.85	11.04	8.18–14.51	6.33	–	3.82	2.51	This work
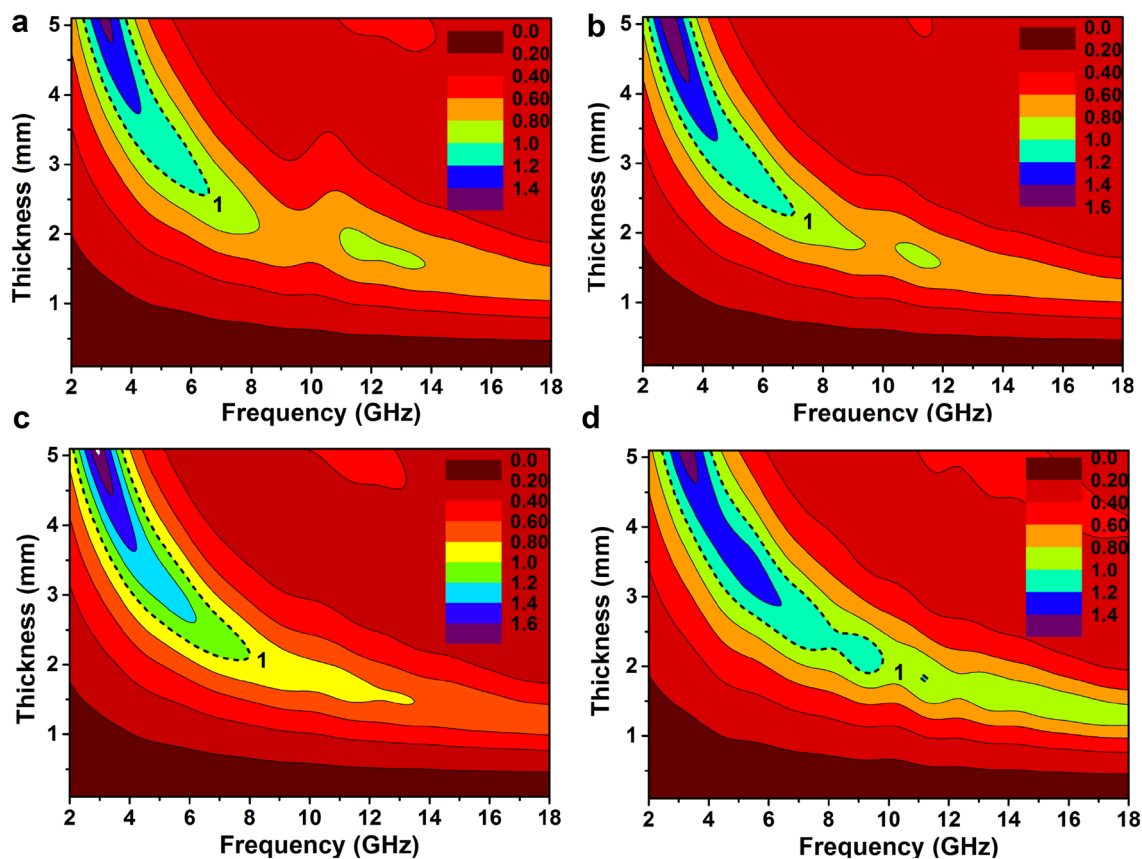
Fig. 8 Contour maps of |Z| at different *f* and *d* for sample **a**: S1, **b**: S2, **c**: S3, and **d**: S4. The black dashed curve indicates |Z| = 1.0

Compliance with ethical standards

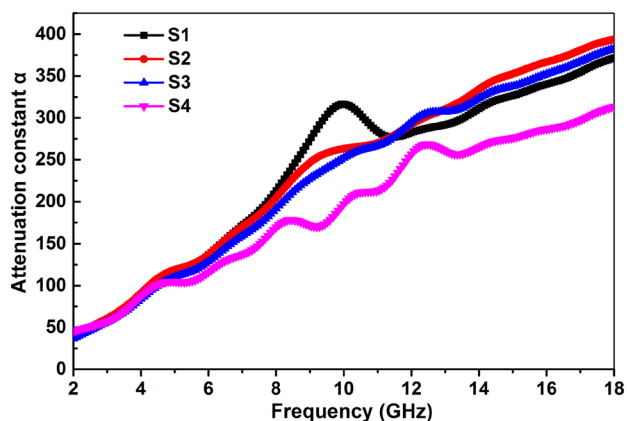**Conflicts of interest** The authors declare that they have no conflicts of interest.

Fig. 9 Attenuation constant *α* as a function of *f* for S1, S2, S3 and S4 samples mixed with paraffin

References

1. M.S. Cao, Y.Z. Cai, P. He, J.C. Shu, W.Q. Cao, J. Yuan, 2D MXenes: electromagnetic property for microwave absorption and electromagnetic interference shielding. Chem. Eng. J. **359**, 1265–1302 (2019)

2. J.T. Feng, Y.H. Hou, Y.C. Wang, L.C. Li, Synthesis of hierarchical ZnFe$_2$O$_4$@SiO$_2$@RGO core-shell microspheres for enhanced electromagnetic wave absorption. ACS Appl. Mater. Interfaces. **9**, 14103–14111 (2017)

3. B. Zhao, X.Q. Guo, W.Y. Zhao, J.S. Deng, G. Shao, B.B. Fan, Z.Y. Bai, R. Zhang, Yolk-shell Ni@SnO$_2$ composites with a designable interspace to improve the electromagnetic wave absorption properties. ACS Appl. Mater. Interfaces. **8**, 28917–28925 (2016)

4. K. Baek, S.Y. Lee, S.G. Doh, M. Kim, J.K. Hyun, Axial oxygen vacancy-regulated microwave absorption in micron-sized tetragonal BaTiO$_3$ particles. J. Mater. Chem. C **6**, 9749–9755 (2018)

5. A.N. Hapishah, M.M. Syazwan, M.N. Hamidon, Synthesis and characterization of magnetic and microwave absorbing properties in polycrystalline cobalt zinc ferrite (Co$_{0.5}$Zn$_{0.5}$Fe$_2$O$_4$) composite. J. Mater. Sci. **29**, 20573–20579 (2018)

6. L. Quan, F.X. Qin, D. Estevez, W. Lu, H. Wang, H.X. Peng, The role of graphene oxide precursor morphology in magnetic and microwave absorption properties of nitrogen-doped graphene. J. Phys. D **52**, 305001 (2019)

7. W.L. Song, L.Z. Fan, Z.L. Hou, K.L. Zhang, Y.B. Ma, M.S. Cao, A wearable microwave absorption cloth. J. Mater. Chem. C **5**, 2432–2441 (2017)

8. R.G. Liu, Y.X. Li, C.H. Li, J.Y. Wang, Z.H. Wang, Y.H. Zhang, F. Qi, X.F. Zhang, High performance microwave absorption through multi-scale metacomposite by intergrating Ni@C nanocapsules with millimetric polystyrene sphere. J. Phys. D **51**, 365303 (2018)

9. M. Rahimi-Nasrabadi, M.H. Mokarian, M.R. Ganjali, M.A. Kashi, S.A. Arani, Synthesis, characterization, magnetic and microwave absorption properties of iron–cobalt nanoparticles and iron–cobalt@polyaniline (FeCo@PANI) nanocomposites. J. Mater. Sci. **29**, 12126–12134 (2018)

10. Y. Huang, J.D. Ji, Y. Chen, X. Li, J. He, X.W. Cheng, S.L. He, Y. Liu, J.P. Liu, Broadband microwave absorption of Fe_3O_4–$BaTiO_3$ composites enhanced by interfacial polarization and impedance matching. Compos. Part B **163**, 598–605 (2019)

11. C.G. Hu, Z.Y. Mou, G.W. Lu, N. Chen, Z.L. Dong, M.J. Hu, L.T. Qu, 3D graphene-Fe_3O_4 nanocomposites with high-performance microwave absorption. Phys. Chem. Chem. Phys. **15**, 13038–13043 (2013)

12. Y.S. Kim, Y.H. Kim, Application of ferro-cobalt magnetic fluid for oil sealing. J. Magn. Magn. Mater. **267**, 105–110 (2003)

13. H. Chiriac, M. Tibu, A.E. Moga, D.D. Herea, Magnetic GMI sensor for detection of biomolecules. J. Magn. Magn. Mater. **293**, 671–676 (2005)

14. G.X. Tong, J.H. Yuan, W.H. Wu, Q. Hu, H.S. Qian, L.C. Li, J.P. Shen, Flower-like Co superstructures: morphology and phase evolution mechanism and novel microwave electromagnetic characteristics. CrystEngComm **14**, 2071–2079 (2012)

15. D.W. Xu, J.L. Liu, P. Chen, Q. Yu, J. Wang, S. Yang, X. Guo, In situ growth and pyrolysis synthesis of super-hydrophobic graphene aerogels embedded with ultrafine β-Co nanocrystals for microwave absorption. J. Mater. Chem. C **7**, 3869–3880 (2019)

16. H. Li, Z. Jin, H.Y. Song, S.J. Liao, Synthesis of Co submicrospheres self-assembled by Co nanosheets via a complexant-assisted hydrothermal approach. J. Magn. Magn. Mater. **322**, 30–35 (2010)

17. L. Guo, F. Liang, N. Wang, D.S. Kong, W.S. Ming, L. He, C.P. Chen, X.M. Meng, Z.Y. Wu, Preparation and characterization of ring-shaped Co nanomaterials. Chem. Mater. **20**, 5163–5168 (2008)

18. Y.J. Zhang, Y. Zhang, Z.H. Wang, D. Li, T.Y. Cui, W. Liu, Z.D. Zhang, Controlled synthesis of cobalt flowerlike architectures by a facile hydrothermal route. Eur. J. Inorg. Chem. **2008**, 2733–2738 (2008)

19. H.T. Yang, C.M. Shen, N.N. Song, Y.M. Wang, T.Z. Yang, H.J. Gao, Z.H. Cheng, Facile synthesis of hollow nano-spheres and hemispheres of cobalt by polyol reduction. Nanotechnology **21**, 375602 (2010)

20. C.Z. He, S. Qiu, X.Z. Wang, J.R. Liu, L.Q. Luan, W. Liu, M. Itoh, K. Machida, Facile synthesis of hollow porous cobalt spheres and their enhanced electromagnetic properties. J. Mater. Chem. **22**, 22160–22166 (2012)

21. G.H. Pan, J. Zhu, S.L. Ma, G.B. Sun, X.J. Yang, Enhancing the electromagnetic performance of Co through the phase-controlled synthesis of hexagonal and cubic Co nanocrystals grown on graphene. ACS Appl. Mater. Interfaces. **5**, 12716–12724 (2013)

22. J.S. Deng, S.M. Li, Y.Y. Zhou, L.Y. Liang, B. Zhao, X. Zhang, R. Zhang, Enhancing the microwave absorption properties of amorphous CoO nanosheet-coated Co (hexagonal and cubic phases) through interfacial polarizations. J. Colloid Interface Sci. **509**, 406–413 (2018)

23. R.L. Ji, C.B. Cao, Z. Chen, H.Z. Zhai, J. Bai, Solvothermal synthesis of $Co_xFe_{3-x}O_4$ spheres and their microwave absorption properties. J. Mater. Chem. C **2**, 5944–5953 (2014)

24. J.W. Wang, X. Wang, Q. Peng, Y.D. Li, Synthesis and characterization of bismuth single-crystalline nanowires and nanospheres. Inorg. Chem. **43**, 7552–7556 (2004)

25. J. Chatterjee, M. Bettge, Y. Haik, C.J. Chen, Synthesis and characterization of polymer encapsulated Cu–Ni magnetic nanoparticles for hyperthermia applications. J. Magn. Magn. Mater. **293**, 303–309 (2005)

26. M.Y. Guan, J.H. Sun, C.L. Gao, X. Li, Z. Xu, A novel cobalt submicro-wire network and its magnetic properties. ChemPhysChem **8**, 2182–2184 (2007)

27. S.H. Yang, J.G. Yang, B.P. Zhang, Y.F. Chen, M.T. Tang, Preparation of ultrafine spheric Co powder by polyot reduction. J. Jishou Univ. (Nat. Sci. Ed.) **25**, 30–34 (2004)

28. Y.C. Zhu, H.G. Zheng, Q. Yang, A.L. Pan, Z.P. Yang, Y.T. Qian, Growth of dendritic cobalt nanocrystals at room temperature. J. Cryst. Growth **260**, 427–434 (2004)

29. R. Yao, S.Y. Liao, C.L. Dai, Y.C. Liu, X.Y. Chen, F. Zheng, Preparation and characterization of novel glass–ceramic tile with microwave absorption properties from iron ore tailings. J. Magn. Magn. Mater. **378**, 367–375 (2015)

30. H.Q. Zhao, Y. Cheng, W. Liu, Z.Z. Yang, B.S. Zhang, G.B. Ji, Y.W. Du, The flaky porous Fe_3O_4 with tunable dimensions for enhanced microwave absorption performance in X and C bands. Nanotechnology **29**, 295603 (2018)

31. X.B. Xie, Y. Pang, H. Kikuchi, T. Liu, The synergistic effects of carbon coating and micropore structure on the microwave absorption properties of Co/CoO nanoparticles. Phys. Chem. Chem. Phys. **18**, 30507–30514 (2016)

32. S.L. Wen, Y. Liu, X.C. Zhao, J.W. Cheng, H. Li, Facile synthesis of novel cobalt particles by reduction method and their microwave absorption properties. Powder Technol. **264**, 128–132 (2014)

33. A. Khort, K. Podbolotov, R. Serrano-Garcia, Y. Gun'ko, One-step solution combustion synthesis of cobalt nanopowder in air atmosphere: the fuel effect. Inorg. Chem. **57**, 1464–1473 (2018)

34. X.F. Dong, M. Qi, Y. Tong, F. Ye, Solvothermal synthesis of single-crystalline hexagonal cobalt nanofibers with high coercivity. Mater. Lett. **128**, 39–41 (2014)

35. S.L. Wen, Y. Liu, X.C. Zhao, Z.Z. Fan, Synthesis, permeability resonance and microwave absorption of flake-assembled cobalt superstructure. J. Magn. Magn. Mater. **385**, 182–187 (2015)

36. W.S. Sun, H. Li, Y. Liu, X.C. Zhao, J.W. Cheng, S.L. Wen, Preparation and microwave absorption properties of spherical cobalt particles. Rare Metal Mater. Eng. **45**, 3099–3103 (2016)

37. M.L. Yang, Y. Yuan, W.L. Yin, S. Yang, Q.Y. Peng, J.J. Li, Y.B. Li, X.D. He, Co/CoO@C nanocomposites with a hierarchical bowknot-like nanostructure for high performance broadband electromagnetic wave absorption. Appl. Surf. Sci. **469**, 607–616 (2019)

38. J.S. Deng, X. Zhang, B. Zhao, Z.Y. Bai, S.M. Wen, S.M. Li, S.Y. Li, J. Yang, R. Zhang, Fluffy microrods to heighten the microwave absorption properties through tuning the electronic state of Co/CoO. J. Mater. Chem. C **6**, 7128–7140 (2018)

39. D.W. Liu, Y.C. Du, Z.N. Li, Y.H. Wang, P. Xu, H.H. Zhao, F.Y. Wang, C.L. Li, X.J. Han, Facile synthesis of 3D flower-like Ni microspheres with enhanced microwave absorption properties. J. Mater. Chem. C **6**, 9615–9623 (2018)

40. T. Shang, Q.S. Lu, L.M. Chao, Y.L. Qin, Y.H. Yun, G.H. Yun, Effects of ordered mesoporous structure and La-doping on the microwave absorbing properties of $CoFe_2O_4$. Appl. Surf. Sci. **434**, 234–242 (2018)

41. Y.B. Li, X.B. Zhou, J. Wang, Q.H. Deng, M.A. Li, S.Y. Du, Y.H. Han, J. Lee, Q. Huang, Facile preparation of in situ coated $Ti_3C_2T_x$/$Ni_{0.5}Zn_{0.5}Fe_2O_4$ composites and their electromagnetic performance. RSC Adv. **7**, 24698–24708 (2017)

42. Z.Z. Wang, H. Bi, P.H. Wang, M. Wang, Z.W. Liu, L. Shen, X.S. Liu, Magnetic and microwave absorption properties of self-assemblies composed of core-shell cobalt-cobalt oxide nanocrystals. Phys. Chem. Chem. Phys. **17**, 3796–3801 (2015)

43. N.N. Song, H.T. Yang, H.L. Liu, X. Ren, H.F. Ding, X.Q. Zhang, Z.H. Cheng, Exceeding natural resonance frequency limit of monodisperse Fe_3O_4 nanoparticles via superparamagnetic relaxation. Sci. Rep. **3**, 3161 (2013)

44. J.S. Deng, Q.B. Wang, Y.Y. Zhou, B. Zhao, R. Zhang, Facile design of a ZnO nanorod–Ni core–shell composite with dual peaks to tune its microwave absorption properties. RSC Adv. **7**, 9294–9302 (2017)

45. M.Z. Wu, Y.D. Zhang, S. Hui, T.D. Xiao, S.H. Ge, W.A. Hines, J.I. Budnick, G.W. Taylor, Microwave magnetic properties of $Co_{50}/(SiO_2)_{50}$ nanoparticles. Appl. Phys. Lett. **80**, 4404–4406 (2002)

46. J.G. Li, J.J. Huang, Y. Qin, F. Ma, Magnetic and microwave properties of cobalt nanoplatelets. Mater. Sci. Eng., B **138**, 199–204 (2007)

47. X.L. Shi, M.S. Cao, J. Yuan, X.Y. Fang, Dual nonlinear dielectric resonance and nesting microwave absorption peaks of hollow cobalt nanochains composites with negative permeability. Appl. Phys. Lett. **95**, 163108 (2009)

48. F. Ma, Y. Qin, Y.Z. Li, Enhanced microwave performance of cobalt nanoflakes with strong shape anisotropy. Appl. Phys. Lett. **96**, 202507 (2010)

49. X. Liu, Y.L. Qiu, Y.T. Ma, H.F. Zheng, L.S. Wang, Q.F. Zhang, Y.Z. Chen, D.L. Peng, Facile preparation and microwave absorption properties of porous Co/CoO microrods. J. Alloys Compd. **721**, 411–418 (2017)

50. S.L. Wen, X.C. Zhao, Y. Liu, J.W. Cheng, H. Li, Synthesis of hierarchical sword-like cobalt particles and their microwave absorption properties. RSC Adv. **4**, 40456–40463 (2014)